LETTER

Circular polarization in the optical afterglow of GRB 121024A

K. Wiersema[1], S. Covino[2], K. Toma[3,4,5], A. J. van der Horst[6], K. Varela[7], M. Min[6], J. Greiner[7], R. L. C. Starling[1], N. R. Tanvir[1], R. A. M. J. Wijers[6], S. Campana[2], P. A. Curran[8], Y. Fan[9], J. P. U. Fynbo[10], J. Gorosabel[11,12,13], A. Gomboc[14], D. Götz[15], J. Hjorth[10], Z. P. Jin[9], S. Kobayashi[16], C. Kouveliotou[17], C. Mundell[16], P. T. O'Brien[1], E. Pian[18,19], A. Rowlinson[6], D. M. Russell[20,21,22], R. Salvaterra[23], S. di Serego Alighieri[24], G. Tagliaferri[2], S. D. Vergani[2], J. Elliott[7], C. Fariña[25], O. E. Hartoog[6], R. Karjalainen[25], S. Klose[26], F. Knust[7], A. J. Levan[27], P. Schady[7], V. Sudilovsky[7] & R. Willingale[1]

Gamma-ray bursts (GRBs) are most probably powered by collimated relativistic outflows (jets) from accreting black holes at cosmological distances. Bright afterglows are produced when the outflow collides with the ambient medium. Afterglow polarization directly probes the magnetic properties of the jet when measured minutes after the burst, and it probes the geometric properties of the jet and the ambient medium when measured hours to days after the burst[1–5]. High values of optical polarization detected minutes after the burst of GRB 120308A indicate the presence of large-scale ordered magnetic fields originating from the central engine[5] (the power source of the GRB). Theoretical models predict low degrees of linear polarization and no circular polarization at late times[6–8], when the energy in the original ejecta is quickly transferred to the ambient medium and propagates farther into the medium as a blast wave. Here we report the detection of circularly polarized light in the afterglow of GRB 121024A, measured 0.15 days after the burst. We show that the circular polarization is intrinsic to the afterglow and unlikely to be produced by dust scattering or plasma propagation effects. A possible explanation is to invoke anisotropic (rather than the commonly assumed isotropic) electron pitch-angle distributions, and we suggest that new models are required to produce the complex microphysics of realistic shocks in relativistic jets[9–11].

Magnetic fields play a crucial role in the physics of relativistic jets—for example, in their formation, acceleration and collimation[1,12,13]. On smaller spatial scales, there is a strong connection between particle acceleration and magnetic field generation in the collisionless relativistic shocks that create GRB afterglows[9–11]. Our understanding of magnetic field properties in GRBs and their afterglows has improved rapidly through recent observational successes, such as time-resolved linear polarimetry of prompt γ-ray emission[14,15] (just seconds after the burst) and the observed transition of reverse shock emission (high levels of optical linear polarization, seen just minutes after the burst) to the early forward shock afterglow emission (lower levels of linear polarization)[5]. These observations have given support to models predicting large-scale ordered fields in the GRB ejecta[5]. On the other hand, late-time polarimetry (hours to days after the burst) offers the advantage that at these times the optical emission probably originates from a single emission process, namely synchrotron emission from the forward shock (that is, emission from the shocked ambient medium), in which ordered fields are much less likely to be present[5]. This then allows measurements of the geometry of the jet through monitoring of the late-time polarization angle[2–4,16,17], but crucially also offers a simple test for afterglow microphysics via circular polarimetry—detailed models have been developed, but observational attempts have largely focused on radio reverse shocks, producing only upper limits[18], and a single optical non-detection[17].

GRB 121024A was detected by the Burst Alert Telescope (BAT) on board the Swift satellite at 02:56:12 UT on 24 October 2012[19]; a redshift of $z = 2.298$ was determined shortly afterwards (Methods). We obtained imaging polarimetry observations with the FOcal Reducer and low dispersion Spectrograph (FORS2) on the Very Large Telescope (VLT), using a Wollaston prism and quarter- and half-wavelength plates (Extended Data Figs 1 and 2). Observations with the ESO R_{special} filter commenced at 2.57 h after the burst, when the afterglow had an R-band brightness of $R \approx 19.8$ mag. After two sets of linear polarimetry (giving the percentage of linear polarization, P_{lin}), we obtained four consecutive measurements of the percentage of circular polarization (P_{cir}), followed by a further 9 measurements of P_{lin} (of which 4 were on the second night). Data reduction and calibration follow standard procedures[17] (Methods). Simultaneously with the polarimetry, we monitored the afterglow optical light curve with the Gamma-Ray Burst Optical/Near-Infrared Detector (GROND) instrument (Methods). In the following we will use a notation where the flux density F depends on frequency v and time t as $F \propto t^{-\alpha} v^{-\beta}$, with temporal decay index α and spectral energy index β.

The X-ray light curve obtained by Swift (retrieved from the online Swift/XRT GRB light curve repository[20]) is well described by three power-law segments, where the first break occurs at $t_{\mathrm{break},1} = 619^{+199}_{-348}$ s and the second break at $t_{\mathrm{break},2} = 3.4^{+1.5}_{-2.2} \times 10^4$ s (errors at 90% confidence level). In the GROND light curve, we find evidence of a break at a time consistent with this last X-ray break (Extended Data Fig. 3). A combined fit to the X-ray and GROND data, using a smoothly broken power law and a host galaxy component, gives a best-fitting break time $t_{\mathrm{break},2} = 3.72 \pm 0.07 \times 10^4$ s (Methods), pre-break light-curve decay indices $\alpha_{\mathrm{pre,opt}} = 0.93 \pm 0.02$ and $\alpha_{\mathrm{pre,X-ray}} = 0.96 \pm 0.11$, and post-break light-curve decay indices $\alpha_{\mathrm{post,opt}} = 1.25 \pm 0.04$ and $\alpha_{\mathrm{post,X-ray}} = 1.67 \pm 0.10$ (uncertainties

[1]Department of Physics and Astronomy, University of Leicester, Leicester LE1 7RH, UK. [2]INAF/Brera Astronomical Observatory, via Bianchi 46, I-23807 Merate (LC), Italy. [3]Department of Earth and Space Science, Osaka University, Toyonaka 560-0043, Japan. [4]Astronomical Institute, Tohoku University, Sendai 980-8578, Japan. [5]Frontier Research Institute for Interdisciplinary Sciences, Tohoku University, Sendai 980-8578, Japan. [6]Astronomical Institute 'Anton Pannekoek', University of Amsterdam, PO Box 94248, 1090 SJ Amsterdam, The Netherlands. [7]Max-Planck-Institut für extraterrestrische Physik, Giessenbachstrasse 1, D-85748 Garching, Germany. [8]International Centre for Radio Astronomy Research, Curtin University, GPO Box U1987, Perth, Western Australia 6845, Australia. [9]Key Laboratory of Dark Matter and Space Astronomy, Purple Mountain Observatory, Chinese Academy of Science, Nanjing 210008, China. [10]Dark Cosmology Centre, Niels Bohr Institute, University of Copenhagen, Juliane Maries Vej 30, DK 2100 Copenhagen, Denmark. [11]Instituto de Astrofísica de Andalucía (IAA-CSIC), Glorieta de la Astronomía s/n, E-18008 Granada, Spain. [12]Unidad Asociada Grupo Ciencia Planetarias UPV/EHU-IAA/CSIC, Departamento de Física Aplicada I, ETS Ingeniería, Universidad del País Vasco UPV/EHU, Alameda de Urquijo s/n, E-48013 Bilbao, Spain. [13]Ikerbasque, Basque Foundation for Science, Alameda de Urquijo 36-5, E-48008 Bilbao, Spain. [14]Faculty of Mathematics and Physics, University of Ljubljana, Jadranska 19, 1000 Ljubljana, Slovenia. [15]AIM (UMR 7158 CEA/DSM-CNRS-Université Paris Diderot) Irfu/Service d'Astrophysique, Saclay, F-91191 Gif-sur-Yvette Cedex, France. [16]Astrophysics Research Institute, Liverpool John Moores University, Liverpool Science Park, IC2 Building, 146 Brownlow Hill, Liverpool L3 5RF, UK. [17]Space Science Office, ZP12, NASA/Marshall Space Flight Center, Huntsville, Alabama 35812, USA. [18]Scuola Normale Superiore, 7, I-56126 Pisa, Italy. [19]INAF/IASF Bologna, via Gobetti 101, I-40129 Bologna, Italy. [20]Instituto de Astrofísica de Canarias (IAC), E-38200 La Laguna, Tenerife, Spain. [21]Departamento de Astrofísica, Universidad de La Laguna, E-38206 La Laguna, Tenerife, Spain. [22]New York University Abu Dhabi, PO Box 129188, Abu Dhabi, United Arab Emirates. [23]INAF/IASF Milano, via E. Bassini 15, 20133 Milano, Italy. [24]INAF-Osservatorio Astrofisico di Arcetri, Largo E. Fermi 5, I-50125 Firenze, Italy. [25]Isaac Newton Group of Telescopes, Apartado de Correos 321, E-38700 Santa Cruz de la Palma, Canary Islands, Spain. [26]Thüringer Landessternwarte Tautenburg, Sternwarte 5, 07778 Tautenburg, Germany. [27]Department of Physics, University of Warwick, Coventry CV4 7AL, UK.
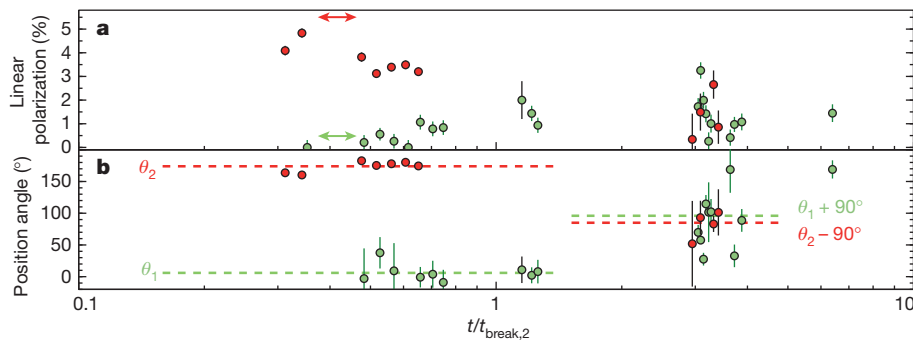
Figure 1 | Linear polarization of the afterglow of GRB 121024A. a, The percentage of linear polarization as a function of time; **b**, the polarization angle. Red points are for GRB 121024A, green points are for the only other Swift GRB afterglow with extensive polarimetry, GRB 091018[17] (error bars are 1σ). The horizontal axis marks the time since trigger, normalized by the jet break time

($t_{break,2} = 3.72 \pm 0.07 \times 10^4$ s). θ_1 and θ_2 show the average angles before the jet break; $\theta_{1,2} + 90$ demonstrates the $90°$ angle change predicted for jet breaks of uniform jets. Horizontal double-headed arrows show the timespan over which the circular polarimetry was obtained.

are 1σ). The occurrence of a light-curve break simultaneously in X-ray and optical wavelengths is suggestive of a jet break origin: a late-time, usually achromatic, light-curve break, generally associated with the finite opening angle of the jet that becomes apparent when the jet Lorentz factor decreases below a critical value. The X-ray + GROND spectral energy distribution is best fitted with a single power law with $\beta = 0.88 \pm 0.01$ and an optical extinction $A_V = 0.22 \pm 0.02$ mag (Methods; Extended Data Fig. 4). The pre-break temporal and spectral indices agree with the standard fireball closure relations[21] in the situation where the synchrotron cooling frequency ν_c and peak frequency ν_m are below both optical and X-ray frequencies[21].

Figure 1 shows the observed P_{lin} behaviour. Initially the source starts out ~5% polarized (much lower than the ~70% expected for a perfectly ordered magnetic field); this polarization subsequently decays to lower levels, while the polarization angle is remarkably constant. This shows that the magnetic field directions are largely random, that is, the coherence scales of the field in the blast wave are small, but their directions are confined to the plane of the shock (the detected polarization is attributed to a somewhat off-axis viewing angle). In the second night of data, the polarization angle is markedly different, consistent (within errors) with a change of exactly $90°$ (Fig. 1). We consider this an unambiguous detection of the $90°$ angle change predicted to occur around the jet break time of a homogeneous jet that is not spreading sideways[4]. The exact time at which the angle change occurs is dictated by viewing angle[4]. The observed angle change shows that any ordered magnetic fields in the forward shock are weak, if present[22].

We acquired the P_{cir} measurements shown in Fig. 2 between the second and third P_{lin} datapoints. Under the assumption that during this interval no variability in P_{cir} is expected (the time covered is small compared to the time after the burst), we combine the 4 measurements together, and measure $P_{cir} = 0.61\% \pm 0.13\%$ (see Methods). We estimate the percentage of linear polarization during the circular polarimetry interval to be $P_{lin} \approx 4\%$: the afterglow shows a ratio $P_{cir}/P_{lin} \approx 0.15$, several orders of magnitude above basic model predictions (~10^{-4} at optical wavelengths[6–8]; see Methods) and other measured relativistic jet sources[23] (Fig. 3).

A high level of circular polarization can be intrinsic to the source (for example, the P_{cir} of the synchrotron emission from the source) or have its origin in propagation effects within the source (for example, Faraday conversion $P_{lin} \rightarrow P_{cir}$, which is effective in a hot, relativistic medium) or by dust scattering effects along the line of sight. Plasma propagation effects within the source have been shown to be strong at long wavelengths (close to the synchrotron self-absorption frequency, ν_a), but negligible at optical wavelengths[6–8]: it is very unlikely that these effects play a role here.

The influence of dust is limited to the host galaxy, as the Galactic extinction towards GRB 121024A is very small, $E(B - V) = 0.10$ (Methods). Dust affects optical P_{cir} through four possible routes: multiple scattering in an optically thick medium of dust grains; dichroic scattering by

(somewhat aligned) non-spherical dust grains; dichroic extinction of linearly polarized radiation by (somewhat aligned) non-spherical dust grains; and the scattering of linearly polarized radiation by randomly oriented dust particles (if the polarization is not in, or perpendicular to, the scattering plane). The P_{cir} expected to be caused by the last three effects depends strongly on the degree of alignment, source inclination and the total amount of dust involved, for which line-of-sight extinction may be a proxy[24,25]. The weak line-of-sight host galaxy extinction, $A_V = 0.22 \pm 0.02$ mag (Methods), argues against multiple-scattering effects[25]. To rule out the other possibilities, we simulated the efficiency of conversion of $P_{lin} \rightarrow P_{cir}$ through single dust scattering (that is, where each photon has been scattered at most once by a dust particle), finding maximal conversion values at high and low scattering angle regimes of ~10% at ~$100°$, and ~8% at ~$20°$. Models based on partially aligned dust grains have lower efficiency. If a large part of P_{cir} is in fact due to dust, we expect a large fraction, if not all, of the P_{lin} to be caused by dust scattering too. The linear polarization curve (Fig. 1) shows no signs of this: we would not expect to see a constant angle before the jet break (at $t_{break,2}$), nor for P_{lin} to reach near zero at any point, nor a clear $90°$ angle change over the jet break[26]. In addition, light scattered at large scattering angles has not had time to reach us yet (dust very close to the GRB gets destroyed by the GRB prompt emission). After eliminating plasma propagation effects and dust scattering, we therefore conclude that the measured P_{cir} is likely to be largely or fully intrinsic to the afterglow. It is of some interest to compare this with the only other afterglow with deep measurements,
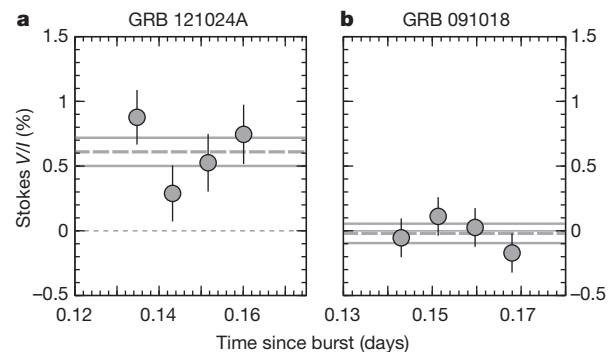

Figure 2 | Optical circular polarization measurements of the afterglow of GRB 121024A. a, Optical circular polarimetry of the afterglow of GRB 121024A; **b**, optical circular polarimetry for GRB 091018[17] (error bars are 1σ). The horizontal axis shows the time since burst in the observer frame, and the vertical axis shows the circular polarization expressed in Stokes parameters V and I (see Methods) as V/I, in per cent. The short-dashed line indicates $V/I = 0$, the dashed line shows the measured V/I from the combined data points, and 1σ uncertainty values around the best combined data value are shown with solid lines.
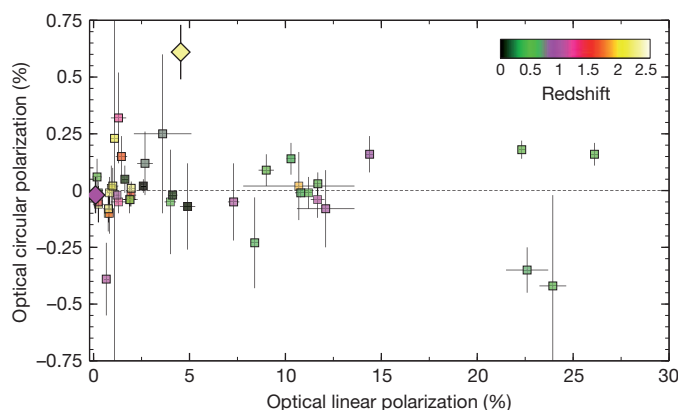
Figure 3 | Optical polarimetry of quasars and GRB afterglows compared.
Polarization measurements for GRBs 121024A and 091018 (diamond symbols) are shown with optical polarimetry of quasars[23] (squares); error bars are 1σ. The data points are colour-coded for redshift. The few quasars with $>3\sigma$ detection of optical circular polarization have high values ($\geq 20\%$) of linear polarization. GRB 121024A has the highest detected level of optical circular polarization, and at $z = 2.298$ is the highest-redshift object with a detection, showing the potential for GRBs as probes of possible cosmological propagation effects. We note that the range of redshifts means that different rest-frame wavelengths are being compared.

that of GRB 091018, which showed limits[17] $P_{cir} < 0.15\%$ (2σ) and $P_{cir}/P_{lin} < 1$ (Figs 1, 2 and 3).

The origin of the optical circular polarization in the afterglow of GRB 121024A is puzzling. We expect intrinsic polarization from the external shock synchrotron emission of $P_{cir} \approx \gamma_e^{-1}$, where γ_e is the random Lorentz factor of the electrons emitting the optical radiation—under the assumption of isotropic electron pitch-angle distribution and perfectly ordered magnetic field[8] (Methods). In this situation, the observed P_{cir} would imply extremely low values of γ_e. Furthermore, because P_{cir} and P_{lin} are both expected to be reduced from the value for a perfectly ordered field by the field randomness in the same way, the expected P_{cir}/P_{lin} ratio is the same as for a perfectly ordered field, again scaling with γ_e^{-1} in the case of an isotropic electron distribution[8]. Therefore, the observed polarimetric behaviour poses a challenge to the long-standing assumption of isotropic electron pitch-angle distributions in the GRB forward shock afterglow. Pitch-angle anisotropy has been postulated before as a possible explanation of GRB phenomena as varied as steep decay phases in X-ray light curves[27] and spectra of prompt emission[28], but evidence for this has been lacking. Further hints of a more complicated structure of emission and acceleration regions come from observations as varied as high-energy emission in GRBs[29] and fast variability of high-energy emission in quasars[30]. The circular polarization of afterglows from GRBs as well as quasars (Fig. 3) offers a new line of evidence required to guide theoretical studies[9,10].

METHODS SUMMARY

Both linear and circular polarimetry of the afterglow of GRB 121024A were performed using the FORS2 instrument on the VLT, using the $R_{special}$ filter in imaging polarimetry mode, using a Wollaston prism and half- and quarter-wavelength plates. We used four plate angles for linear polarimetry and two for circular polarimetry, in order be able to use beam-switching to reduce systematic errors, and used aperture photometry to measure source fluxes. Measurements from polarimetric sequences taken on the second night after the burst were combined to increase signal-to-noise ratios. We used field stars to measure the linear polarization induced by Galactic dust, fitting the distribution in Stokes Q and U with a two-dimensional Gaussian function. We monitored the optical afterglow brightness in seven photometric filters using the GROND instrument, we fitted the X-ray data from the Swift satellite together with the GROND data with absorbed power laws to establish the presence of a late-time break in the light curve, and we fitted the X-ray/optical spectral energy distribution of the afterglow. Finally, we demonstrated how the observed high level of circular polarization contradicts theoretical estimates, and how

anisotropy in the electron pitch-angle distribution may explain the observed ratio of optical circular to linear polarization.

Online Content Any additional Methods, Extended Data display items and Source Data are available in the online version of the paper; references unique to these sections appear only in the online paper.

1. Piran, T. Magnetic fields in gamma-ray bursts: a short overview. *AIP Conf. Proc.* **784,** 164–174 (2005).
2. Sari, R. Linear polarization and proper motion in the afterglow of beamed gamma-ray bursts. *Astrophys. J.* **524,** L43–L46 (1999).
3. Ghisellini, G. & Lazzati, D. Polarization light curves and position angle variation of beamed gamma-ray bursts. *Mon. Not. R. Astron. Soc.* **309,** L7–L11 (1999).
4. Rossi, E. M., Lazzati, D., Salmonson, J. D. & Ghisellini, G. The polarization of afterglow emission reveals gamma-ray bursts jet structure. *Mon. Not. R. Astron. Soc.* **354,** 86–100 (2004).
5. Mundell, C. G. *et al.* Highly polarized light from stable ordered magnetic fields in GRB 120308A. *Nature* **504,** 119–121 (2013).
6. Matsumiya, M. & Ioka, K. Circular polarization from gamma-ray burst afterglows. *Astrophys. J.* **595,** L25–L28 (2003).
7. Sagiv, A., Waxman, E. & Loeb, A. Probing the magnetic field structure in gamma-ray bursts through dispersive plasma effects on the afterglow polarization. *Astrophys. J.* **615,** 366–377 (2004).
8. Toma, K., Ioka, K. & Nakamura, T. Probing the efficiency of electron-proton coupling in relativistic collisionless shocks through the radio polarimetry of gamma-ray burst afterglows. *Astrophys. J.* **673,** L123–L126 (2008).
9. Spitkovsky, A. Particle acceleration in relativistic collisionless shocks: Fermi process at last? *Astrophys. J.* **682,** L5–L8 (2008).
10. Spitkovsky, A. On the structure of relativistic collisionless shocks in electron-ion plasmas. *Astrophys. J.* **673,** L39–L42 (2008).
11. Hededal, C. B. & Nishikawa, K.-I. The influence of an ambient magnetic field on relativistic collisionless plasma shocks. *Astrophys. J.* **623,** L89–L92 (2005).
12. Pudritz, R. E., Hardcastle, M. J. & Gabuzda, D. C. Magnetic fields in astrophysical jets: from launch to termination. *Space Sci. Rev.* **169,** 27–72 (2012).
13. Lyutikov, M. Magnetocentrifugal launching of jets from discs around Kerr black holes. *Mon. Not. R. Astron. Soc.* **396,** 1545–1552 (2009).
14. Götz, D., Laurent, P., Lebrun, F., Daigne, F. & Bosnjak, Z. Variable polarization measured in the prompt emission of GRB 041219A using IBIS on board INTEGRAL. *Astrophys. J.* **695,** L208–L212 (2009).
15. Yonetoku, D. *et al.* Magnetic structures in gamma-ray burst jets probed by gamma-ray polarization. *Astrophys. J.* **758,** L1–L6 (2012).
16. Greiner, J. *et al.* Evolution of the polarization of the optical afterglow of the γ-ray burst GRB 030329. *Nature* **426,** 157–159 (2003).
17. Wiersema, K. *et al.* Detailed optical and near-infrared polarimetry, spectroscopy and broadband photometry of the afterglow of GRB 091018: polarization evolution. *Mon. Not. R. Astron. Soc.* **426,** 2–22 (2012).
18. Granot, J. & Taylor, G. B. Radio flares and the magnetic field structure in gamma-ray burst outflows. *Astrophys. J.* **625,** 263–270 (2005).
19. Pagani, C. *et al.* GRB 121024A: Swift detection of a burst with an optical counterpart. *GCN Circ.* **13886** (2012).
20. Evans, P. A. *et al.* Methods and results of an automatic analysis of a complete sample of Swift-XRT observations of GRBs. *Mon. Not. R. Astron. Soc.* **397,** 1177–1201 (2009).
21. Sari, R., Piran, T. & Narayan, R. Spectra and lightcurves of gamma-ray burst afterglows. *Astrophys. J.* **497,** L17–L20 (1998).
22. Granot, J. & Königl, A. Linear polarisation in gamma-ray bursts: the case for an ordered magnetic field. *Astrophys. J.* **594,** L83–L87 (2003).
23. Hutsemékers, D., Borguet, B., Sluse, D., Cabanac, R. & Lamy, H. Optical circular polarization in quasars. *Astron. Astrophys.* **520,** L7 (2010).
24. Whitney, B. A. & Wolff, M. J. Scattering and absorption by aligned grains in circumstellar environments. *Astrophys. J.* **574,** 205–231 (2002).
25. Fukue, T. *et al.* Near-infrared circular polarimetry and correlation diagrams in the Orion Becklin-Neugebauer/Kleinman-Low region: contribution of dichroic extinction. *Astrophys. J.* **692,** L88–L91 (2009).
26. Lazzati, D. *et al.* Intrinsic and dust-induced polarization in gamma-ray burst afterglows: the case of GRB 021004. *Astron. Astrophys.* **410,** 823–831 (2003).
27. Beloborodov, A. M., Daigne, F., Mochkovitch, R. & Uhm, Z. L. Is gamma-ray burst afterglow emission intrinsically anisotropic? *Mon. Not. R. Astron. Soc.* **410,** 2422–2427 (2011).
28. Lloyd-Ronning, N. M. & Petrosian, V. Interpreting the behavior of time-resolved gamma-ray burst spectra. *Astrophys. J.* **565,** 182–194 (2002).
29. Kouveliotou, C. *et al.* NuSTAR observations of GRB 130427A establish a single component synchrotron afterglow origin for the late optical to multi-GeV emission. *Astrophys. J.* **779,** L1 (2013).
30. Ghisellini, G., Tavecchio, F., Bodo, G. & Celotti, A. TeV variability in blazars: how fast can it be? *Mon. Not. R. Astron. Soc.* **393,** L16–L20 (2009).

METHODS

Linear and circular polarimetry. GRB 121024A triggered the Burst Alert Telescope (BAT) on board the Swift satellite at 02:56:12 UT on 24 October 2012 (Swift trigger 536580)[19]. We will use this trigger time as t_0 (that is, time since burst of an observation is $t = t_{obs} - t_0$) throughout. The prompt emission shows the burst probably belongs to the class of long bursts, with a duration $t_{90} = 69 \pm 32$ s (ref. 31). An X-ray and optical afterglow was found by the Swift X-ray telescope (XRT) and UV–optical telescope (UVOT)[19]. The redshift, $z = 2.298$, was found through afterglow spectroscopy with the X-shooter instrument on the Very Large Telescope[32]. Based on the initial brightness of the UVOT afterglow[19] we activated our VLT polarimetry programme (programme 090.D-0789, PI Wiersema).

The data acquisition strategy, reduction and analysis closely follows that of our recent paper on GRB 091018[17], which in turn follows the specific recommendations set out for FORS polarimetry[33]. We summarize those methods here, and give additional details specific to the case of GRB121024A.

Observations in the FORS2 $R_{special}$ filter started at 9.2×10^3 s after burst. Following an acquisition image (Extended Data Fig. 1), polarimetry was acquired in imaging polarimetry (IPOL) mode. In this instrument mode, a super-achromatic half- or quarter-wavelength plate is used (for linear and circular polarimetry, respectively), after which a Wollaston prism is used to split the light into two beams, the so-called ordinary and extraordinary beam (hereafter the o and e beam) that have perpendicular polarization. These beams are imaged simultaneously: a slit mask is used to prevent overlap of the two beams on the chip (Extended Data Fig. 2). All linear polarization measurements are obtained using four rotation angles ($0°$, $22.5°$, $45°$ and $67.5°$) of the half-wavelength plate; for the circular polarimetry we used two angles ($-45°$ and $+45°$) of the quarter-wavelength plate. The GRB afterglow was positioned in the middle of the mask opening at the default (on-axis) position for FORS2 observations, on chip 1. A small number of linear polarization measurements were taken with a small dither ($\sim$16 pixels in the Y direction) to eliminate any potential effects of bad pixels/columns; none of these problems were apparent. Extended Data Tables 1 and 2 list the polarimetric observations and their resulting measurements.

Data reduction was done within IRAF, using bias and sky flat frames obtained on the same nights. Analysis of the data was done via aperture photometry, using IRAF scripts developed for this purpose, using the following method. We perform aperture photometry of all point sources present on both FORS2 chip 1 and 2, on the o and e images, using an aperture radius of 1.5 times the on-frame full-width at half-maximum (FWHM) of the point spread function (PSF). The PSF is found via a Gaussian fit on all point source objects, on a per-image basis, and is determined independently for the o and e beam as small differences in PSF shape may occur between the beams, particularly for objects far off-axis. The PSF value was used to set the aperture size; for example, the o beam on chip 1 is the weighted average of the FWHM of all point sources in that chip, and image. The sky subtraction was done using an annulus of inner and outer radii 3 and 4 times the FWHM, respectively. We only included sources for which the sky annulus was fully contained within the mask and showed no signs of saturation. Using this procedure we measured fluxes f_o and f_e for all point-like objects in all frames. Errors were determined using $\sigma_{source}^2 = g^{-1} \times f + \left(n_A + n_A^2/n_B\right)\sigma_B^2/\text{pixel}$, where g is the gain, f the flux (f_o and f_e, source minus the mean background) in the aperture, n_A and n_B the number of pixels in aperture and background region; and σ_B/pixel the variance per pixel in the sky level within the annulus.

The read noise contribution to the errors is negligible in these data. Images are not combined (that is, the depth of coverage per pixel is 1). The purpose of using the four angles for linear polarization, and two for the circular, is that the beams switch, eliminating several systematic errors (for example, flat field defects), resulting in increased reliability[33]. We use the fluxes to derive the normalized flux difference at angle number i as $F_i = (f_{o,i} - f_{e,i})/(f_{o,i} + f_{e,i}) = (f_{o,i} - f_{e,i})/I$. We use the Stokes parameters (U, Q, V, I) to describe the source polarization state, often in normalized form (U/I, Q/I, V/I). These can be expressed in terms of F_i as $Q/I = \frac{2}{N}\sum_{i=0}^{N-1} F_i \cos(i\pi/2)$ and $U/I = \frac{2}{N}\sum_{i=0}^{N-1} F_i \sin(i\pi/2)$, where N is the number of half-wavelength plate positions (four positions in this case)[17,33]. The circular-polarization Stokes parameter V/I is similarly computed as $V/I = \frac{1}{2}(F_{45} - F_{-45})$. The benefit of the multiple angle observations is clear from these equations. Further increasing the accuracy by observing at even more angles (for example, eight angles for linear polarization) is difficult for sources as faint as the afterglow of GRB 121024A—it would lead to observing times for single data points that are close to the polarization variability timescale.

We now proceed to correct for the linear polarization induced by dust in our own Galaxy which, along the line of sight to GRB 121024A, has $E(B - V) = 0.10$ (ref. 34). Using the relation $P_{lin} \leq 0.09 \times E(B - V)$ (ref. 35) this corresponds to a maximum induced polarization of $\sim$0.9%, which may be a noticeable fraction of the

detected polarization. To correct for Galactic-dust-induced polarization, we use the same methods as we used for GRB 091018 (ref. 17): we fit the field star Q, U distribution with a two-dimensional Gaussian function. We use three cuts on the sources entering the distribution: we require a polarimetric error $<0.9\%$, a polarization value below 1.5% and a radial distance to the GRB position smaller than $2.5'$. This last cut is to counter the effects of instrumental polarization: the FORS2 instrument shows a broadly radial instrumental linear polarization pattern, with nil polarization on-axis (where the GRB is positioned), and values increasing with radial distance[33,36,37]. By picking this cut-off we prevent the instrumental pattern from influencing the field objects' Q, U centroid determination too much, while still retaining enough sources for a reliable fit. We note that the number of bright field point sources within the mask is low in the case of GRB 121024A (87 data points from 9 individual stars enter the fit, considerably lower than in the case of GRB 091018; ref. 17), resulting in a somewhat larger uncertainty in the Galactic-dust-induced Q, U value. We find a value of $Q_{Gal} = -0.0020$, $U_{Gal} = -0.0046$. We use the standard deviation of the fitted 2D Gaussian as a measure for the uncertainty on the Galactic-dust-induced Stokes parameters, finding $\sigma_{Q_{Gal}} = 0.0040$, $\sigma_{U_{Gal}} = 0.0043$. We correct the afterglow Q, U values by subtracting the Galactic-dust-induced Q, U values. To facilitate comparison with models, we use the Stokes parameters to express the linear polarization in terms of the polarization degree P_{lin} and polarization angle θ as $P_{lin} = \sqrt{(Q^2 + U^2)}/I$ and $\theta = \frac{1}{2}\arctan(U/Q)$, where coordinates are chosen such that $\theta = 0°$ for North, $\theta = 90°$ for East. In the conversion from Q, U to P_{lin}, θ we account for the effects of polarization bias[38,39] in the same manner as done for the data of GRB 091018[17,33]. We correct the angles θ for the FORS2 instrumental zero angle offset[37]. Similarly we can compute $P_{cir} = \sqrt{(V/I)^2}$: the sign of V/I gives the polarization direction (clockwise or anticlockwise). We note that both the instrument-induced circular polarization and linear to circular polarization crosstalk are well studied for the FORS instruments and far below our detection levels on the optical axis (where the afterglow is positioned)[33,36,37], and as such we expect no instrumental contribution to the detected V/I. A small amount of instrumental circular polarization is expected to be present for sources observed far off-axis[36,37], far from the GRB position. Since there are no bright (but unsaturated) stars near the GRB position, it is therefore not possible to use field sources as secure independent secondary standards[33,36,37]. The circular polarization induced by scattering by the dust in our own Galaxy, with $E(B - V) = 0.10$ and the induced linear polarization values as above, does not contribute significantly to the observed P_{cir} (ref. 40).

In the second night of data, the afterglow of GRB 121024A shows a low level of linear polarization, which means that the uncertainty in the angle θ is relatively large, as $\sigma_\theta = \sigma_{P_{lin}}/2P_{lin}$. Nevertheless a clear difference in angle is visible with respect to the first night of data, consistent with a $90°$ change in polarization angle: the angle changes from $172° \pm 2°$ to $85° \pm 10°$ (Extended Data Table 1). The two first observations have angles somewhat discrepant from the pre-jet break average (Extended Data Table 1). Unfortunately we were not able to acquire infrared polarimetry simultaneous with the R-band polarimetry for scheduling reasons—simultaneous multiwavelength polarimetry is the best way to directly measure polarization induced by scattering off dust particles in the host galaxy[34,40,41]. However, the measured line-of-sight extinction and indeed the linear polarization light curve itself provide sufficient evidence that the host galaxy-dust-induced linear polarization must be small: the measured $A_V \approx 0.22$ mag gives a limit on the induced linear polarization of $<0.7\%$ (assuming a Milky Way-like polarization curve[35]).

Light curves and spectral energy distribution. The Swift XRT light curve is well described by three power-law segments, with parameters (errors at 90% confidence level) $\alpha_1 = 1.78^{+0.49}_{-0.10}$, $t_{break,1} = 619^{+199}_{-348}$ s, $\alpha_2 = 0.83^{+0.13}_{-0.22}$, $t_{break,2} = 3.4^{+1.5}_{-2.2} \times 10^4$ s and $\alpha_3 = 1.70^{+0.27}_{-0.36}$ (ref. 20). The uncertainty in the late break time is relatively large, as there are few data points post-break.

The optical afterglow of GRB 121024A was observed extensively with the seven channel (g', r', i', z', J, H, Ks filters) Gamma-Ray Burst Optical and Near-Infrared Detector (GROND[42]) instrument, mounted on the ESO 2.2-m telescope at La Silla, Chile, providing photometric monitoring simultaneous to the polarimetry (Extended Data Table 3). These GROND observations will be described in more detail in a forthcoming, separate publication, but below we give some properties that are required to interpret the polarimetry. In addition to the GROND data, we observed the position of GRB 121024A with the ACAM instrument on the William Herschel Telescope (WHT) on 15 February 2013 (that is, 114.8 days after burst), with the aim of fixing the flux contribution of the host galaxy to the late-time light curve. We acquired 14×180 s exposures in Sloan r filter in relatively poor seeing conditions ($\sim$1.8″). The resulting image (Extended Data Fig. 1) shows a clear detection of a source at the afterglow position, which we identify as the host galaxy of this GRB, confirming that a late-time detection in GROND data in g, r, i is dominated by the host. Its brightness, $r' = 24.03 \pm 0.20$, places the host at the bright end of the host galaxy luminosity distribution at this redshift[43]. Taking this bright host galaxy magnitude into account, a light-curve break at around the same time as the break in XRT data is

apparent (Extended Data Fig. 3). We perform a joint fit to the XRT and GROND light curves (where only XRT data after the first XRT light-curve break, $t_{\text{break,1}}$, are used) to constrain the break time. We fit using a model that consists of a smoothly broken power law, generally defined as

$$F_\nu(t) = F_\nu(t_{\text{break}}) \left(\left(\frac{t}{t_{\text{break}}} \right)^{\alpha_1 s} + \left(\frac{t}{t_{\text{break}}} \right)^{\alpha_2 s} \right)^{-1/s}$$

where t_{break} is the break time, α_1 and α_2 are pre- and post-break light-curve indices, and s is the break smoothness parameter. The pre- and post-break slopes and break smoothness are free parameters in our fit, and the break time is fixed to be the same for X-ray and optical/infrared wavelengths (that is, an achromatic break, and in addition a host galaxy contribution to the optical and infrared fluxes). This results in an acceptable fit statistic (reduced $\chi^2 = 157.38/132 = 1.192$), and the following parameters (uncertainties are 1σ): break time $t_{\text{break,2}} = 3.72 \pm 0.07 \times 10^4$ s and break smoothness $s = 5.01 \pm 0.01$; pre-break light-curve decay indices $\alpha_{\text{pre,opt}} = 0.93 \pm 0.02$, $\alpha_{\text{pre,X-ray}} = 0.96 \pm 0.11$; post-break light-curve decay indices $\alpha_{\text{post,opt}} = 1.25 \pm 0.04$, $\alpha_{\text{post,X-ray}} = 1.67 \pm 0.10$. We identify this late, achromatic, break $t_{\text{break,2}}$ with a so-called jet break. The resulting fit is shown in Extended Data Fig. 3. While in each optical band there are only a few data points post-break, GROND observes in seven bands simultaneously, making the break significant. The relatively shallow post-break optical decay is probably caused by the combination of bright host and smooth break: by the time the light curve asymptotes to its post-break index it is dominated by host galaxy light.

The line-of-sight extinction in the host galaxy and the spectral slopes are found by fitting an XRT+GROND spectral energy distribution (at time 11,085 s after trigger) with a SMC-like extinction law[44]. The best fit, with reduced $\chi^2 = 1.04$, is obtained by a single power law (a broken power law does not result in significant fit improvement) with parameter $\beta = 0.88 \pm 0.01$, and a optical extinction in the V band of $A_V = 0.22 \pm 0.02$ mag.

The fact that X-ray and optical/infrared wavelengths have the same spectral index and that the pre-break decay indices are (within errors) identical, suggests that X-ray and optical are both in the same spectral regime, likely $\nu > \nu_c$. The achromatic nature of the light-curve break is consistent with a jet break interpretation, supporting our interpretation of the linear polarization behaviour of this afterglow.

Circular polarization of synchrotron emission. The linear and circular polarization degrees of the optically thin synchrotron emission from the electrons with a spectrum given by $N(\gamma_e, \alpha) = K\gamma_e^{-p} f(\alpha)$, where γ_e is the electron Lorentz factor, α is the electron pitch angle and K is the normalization factor, are given by[11,45]

$$P_{\text{lin}} = \frac{p+1}{p+\frac{7}{3}}$$

$$P_{\text{cir}} = \frac{1}{\gamma_e} \frac{(2+p)\cot\theta + g(\theta)}{p} \frac{p+1}{p+\frac{7}{3}} \frac{\Gamma\left(\frac{3p+8}{12}\right)\Gamma\left(\frac{3p+4}{12}\right)}{\Gamma\left(\frac{3p+7}{12}\right)\Gamma\left(\frac{3p-1}{12}\right)}$$

Here θ is the viewing angle with respect to the magnetic field direction, Γ is the mathematical Gamma function, and we have defined

$$g(\theta) \equiv \frac{1}{f(\theta)} \frac{df(\alpha)}{d\alpha}\bigg|_{\alpha=0}$$

These two equations are valid when $g(\theta) \ll \gamma_e$.

If the electron pitch-angle distribution is isotropic, that is, $g(\theta) = 0$, then $P_{\text{cir}} \sim \gamma_e^{-1}$. This simply means that the circular polarization contributions of electrons with pitch angles $\theta + \alpha$ and $\theta - \alpha$ nearly cancel out, and the remaining P_{cir} scales with the angular size of the beaming cone of the synchrotron emission, γ_e^{-1}.

The electrons with Lorentz factor γ_e mainly contribute to the synchrotron emission at frequency $\nu = \left(\frac{eB}{2\pi m_e c} \right) \gamma_e^2 \frac{\Gamma}{1+z}$, where the magnetic field strength B and the blast wave Lorentz factor Γ can be estimated by the standard external shock model[21]. Therefore, by calculating the Lorentz factor of the electrons producing the R-band emission, one can predict P_{cir} at the observing time as

$$P_{\text{cir}} \approx 10^{-4} \varepsilon_{B,-2}^{1/4} E_{52}^{1/8} n^{1/8}$$

where $\varepsilon_B = 0.01\varepsilon_{B,-2}$ is the fraction of the magnetic energy density to the internal energy density, $E = 10^{52} E_{52}$ (erg) is the total blast wave energy and n (cm^{-3}) is the circumburst particle number density. This value does not strongly depend on the model parameters, and is very low (in spite of the assumption that the magnetic field is ordered) compared to the observed value of $P_{\text{cir}} = 0.61 \pm 0.13\%$. In reality, the magnetic field directions are largely random, as implied by the observed P_{lin} light curve. However, the linear and circular polarization degrees are reduced to the same extent by the randomness of the field, so the ratio $P_{\text{cir}}/P_{\text{lin}} \approx 10^{-4}$ is applicable also for the random field case, which is clearly inconsistent with the observed value $P_{\text{cir}}/P_{\text{lin}} \approx 0.15$.

In a situation where the pitch-angle distribution is not isotropic, the circular polarization contributions of electrons are not cancelled out and P_{cir} can be higher. The observed polarization ratio $P_{\text{cir}}/P_{\text{lin}}$, implies that $g(\theta)/\gamma_e \approx 0.1$ and then $g(\theta) \approx 10^3$, which means a highly anisotropic pitch-angle distribution.

The detection of high circular polarization implies that the emitting plasma consists mainly of electrons and protons, rather than electrons and positrons, because the circular polarizations of the synchrotron emission of electrons and positrons perfectly cancel out[45]. This implication is consistent with the emission model of the forward shock propagating in the circumburst medium.

31. Barthelmy, S. D. *et al.* GRB 121024A: Swift-BAT refined analysis. *GCN Circ.* **13889** (2012).
32. Tanvir, N. R. *et al.* GRB121024A: VLT/X-shooter redshift. *GCN Circ.* **13890** (2012).
33. Patat, F. & Romaniello, M. Error analysis for dual-beam optical linear polarimetry. *Publ. Astron. Soc. Pacif.* **118**, 146–161 (2006).
34. Schlegel, D. J., Finkbeiner, D. P. & Davis, M. Maps of dust infrared emission for use in estimation of reddening and cosmic microwave background radiation foregrounds. *Astrophys. J.* **500**, 525–553 (1998).
35. Serkowski, K., Matheson, D. S. & Ford, V. L. Wavelength dependence of interstellar polarisation and ratio of total to selective extinction. *Astrophys. J.* **196,** 261–290 (1975).
36. Bagnulo, S., Szeifert, T., Wade, G. A., Landstreet, J. D. & Mathys, G. Measuring magnetic fields of early-type stars with FORS1 at the VLT. *Astron. Astrophys.* **389,** 191–201 (2002).
37. FORS Users Manual Issue 91.1 (ESO, Doc. no. VLT-MAN-ESO-13100-1543, 2012); available at http://www.eso.org/sci/facilities/paranal/instruments/fors/doc.html.
38. Wardle, J. F. C. & Kronberg, P. P. The linear polarisation of quasi-stellar radio sources at 3.71 and 11.1 centimeters. *Astrophys. J.* **194,** 249–255 (1974).
39. Simmons, J. F. L. & Stewart, B. G. Point and interval estimation of the true unbiased degree of linear polarisation in the presence of low signal-to-noise ratios. *Astron. Astrophys.* **142,** 100–106 (1985).
40. Martin, P. G. Interstellar circular polarisation. *Mon. Not. R. Astron. Soc.* **159,** 179–190 (1972).
41. Klose, S. *et al.* Prospects for multiwavelength polarisation observations of GRB afterglows and the case GRB 030329. *Astron. Astrophys.* **420,** 899–903 (2004).
42. Greiner, J. *et al.* GROND — a 7-channel imager. *Publ. Astron. Soc. Pacif.* **120,** 405–424 (2008).
43. Hjorth, J. *et al.* The optically unbiased gamma-ray burst host (TOUGH) survey. I. Survey design and catalogs. *Astrophys. J.* **756,** 187–202 (2012).
44. Pei, Y. C. Interstellar dust from the Milky Way to the Magellanic Clouds. *Astrophys. J.* **395,** 130–139 (1992).
45. Melrose, D. B. *Non-thermal Processes in Diffuse Magnetised Plasmas* Vol. 1 (Gordon & Breach, 1980).
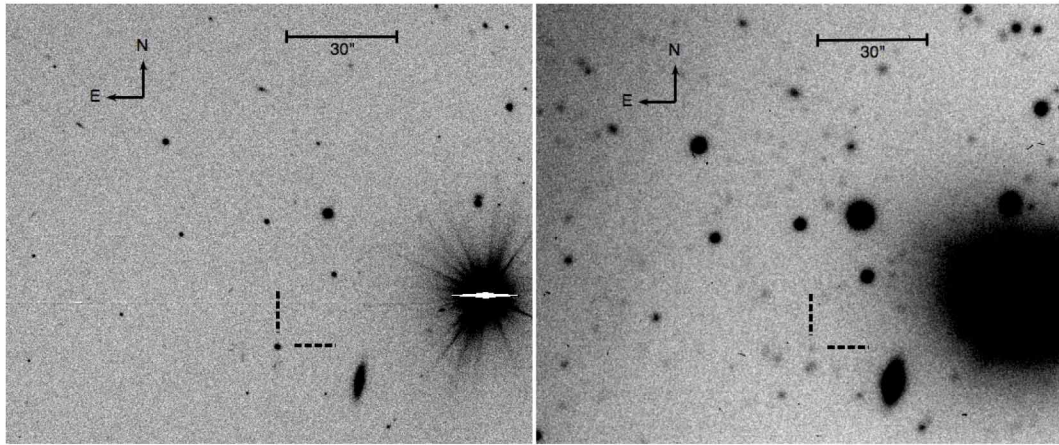
Extended Data Figure 1 | Host galaxy and afterglow image. Left, VLT FORS2 $R_{special}$-band acquisition image, with the afterglow indicated by broken lines. Right, detection of the host galaxy in the late-time WHT ACAM r-band imaging.
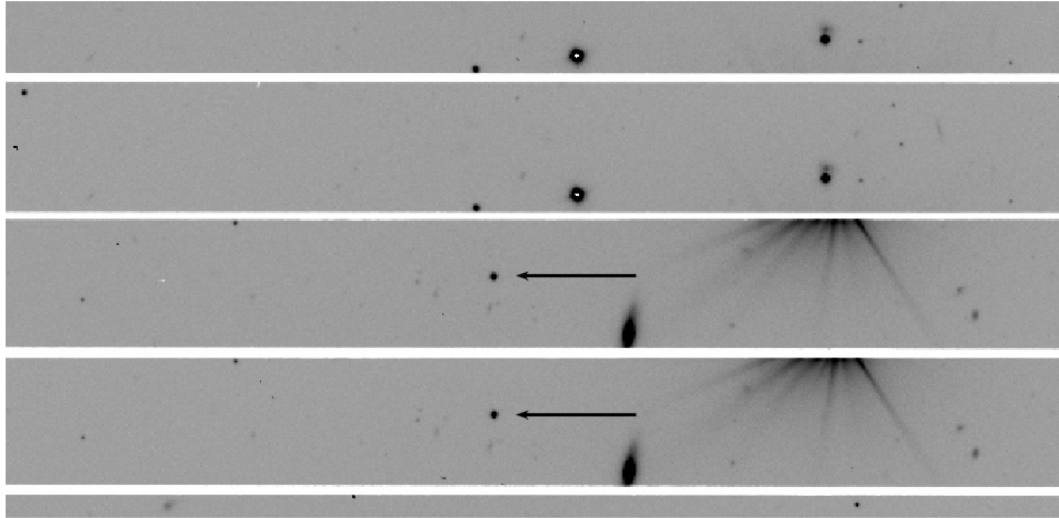
Extended Data Figure 2 | Polarimetry mask and afterglow brightness.
A small section of a single FORS2 $R_{special}$-band polarimetric exposure (this is the $-45°$ angle chip 1 frame of the cir4 set), illustrating the shape of the aperture mask and brightness of the afterglow (indicated by an arrow). Each part of the sky that falls into the open part of the rectangular mask is imaged twice, in perpendicular polarizations, the o and e beams, which is why the same objects each time appear in two non-overlapping strips.
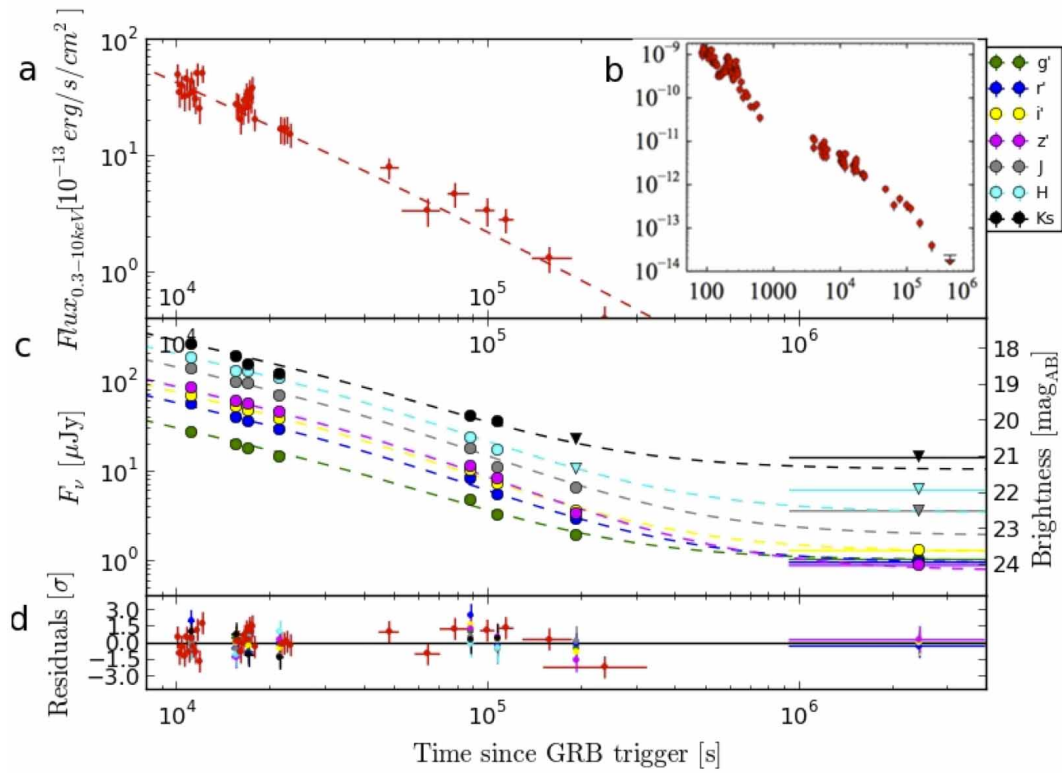
Extended Data Figure 3 | Optical and X-ray afterglow light curves. a, Swift XRT X-ray light curve in the time span covered by GROND observations; **b**, the full XRT light curve. **c**, Full GROND light curves in all seven bands (key at top right). Overplotted in **a** and **c** is the best-fitting smoothly broken power law (Methods), with a host galaxy contribution to the optical data. Residuals of this fit are shown in **d**.
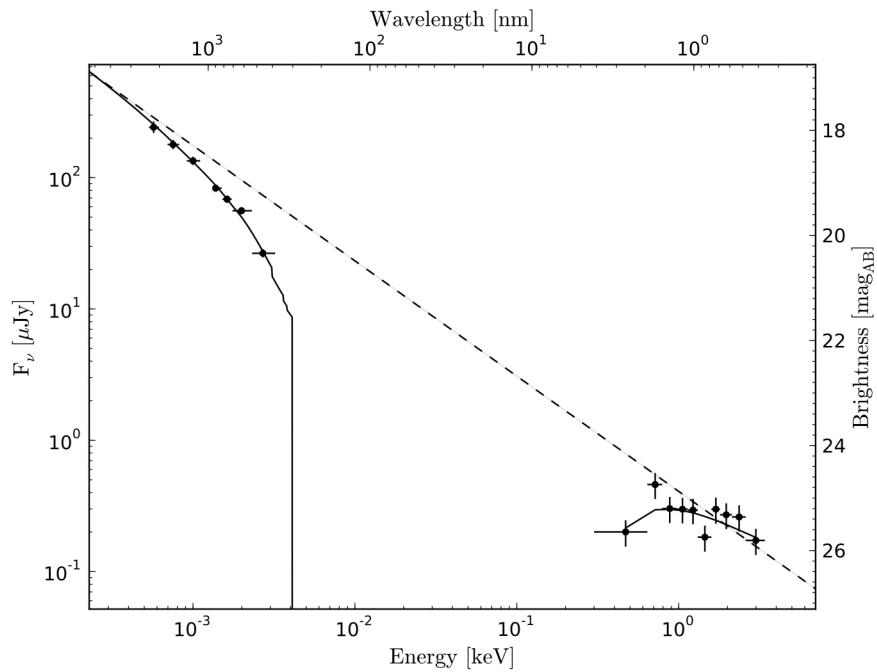
Extended Data Figure 4 | X-ray/optical spectral energy distribution of the afterglow of GRB 121024A. Shown is a spectral energy distribution using the seven GROND photometric bands and simultaneous Swift XRT X-ray data. The overplotted solid line is the best-fitting absorbed power law; the dashed line shows the best-fitting power law without the effects of reddening and X-ray absorption. The horizontal error bars on the optical and X-ray data show the filter throughput and spectral bin-size, respectively. Vertical error bars show 1σ uncertainties on the fluxes.

Extended Data Table 1 | Linear polarimetry results

Datapoint identifier	Time since t_0 (mid; s)	P_{lin} (%)	θ (degrees)	Exposure time
lin1	9698	4.09 ± 0.20	163.7 ± 2.8	4×3 min
lin2	10638	4.83 ± 0.20	160.3 ± 2.3	4×3 min
lin3	14782	3.82 ± 0.20	182.7 ± 3.0	4×4 min
lin4	16042	3.12 ± 0.19	175.3 ± 3.5	4×5 min
lin5	17425	3.39 ± 0.18	178.0 ± 2.9	4×5 min
lin6	18841	3.49 ± 0.18	180.3 ± 3.0	4×5 min
lin7	20227	3.20 ± 0.18	174.5 ± 3.3	4×5 min
lin8	91624	0.34 ± 1.09	51.9 ± 67.5	$3 \times (4 \times 5)$ min
lin9	95828	1.49 ± 0.78	93.1 ± 26.6	$3 \times (4 \times 5)$ min
lin10	103028	2.66 ± 0.60	83.0 ± 12.6	$2 \times (4 \times 5)$ min
lin11	105814	0.86 ± 0.72	101.3 ± 36.4	$2 \times (4 \times 5)$ min

The polarization angle θ follows a standard coordinate convention: north = 0°, east = 90°. The values are corrected for Galactic-dust-induced polarization in Stokes parameter space, and polarization bias corrections are performed. Note that for the lin8–lin11 datapoints, we combine multiple exposure sets together: the polarization is low and the source faint.

Extended Data Table 2 | Circular polarimetry results

Datapoint identifier	Time since t_0 (mid; s)	V/I ($\times 100$)
cir1	11643	0.87 ± 0.21
cir2	12373	0.30 ± 0.21
cir3	13103	0.53 ± 0.22
cir4	13832	0.75 ± 0.23

Each datapoint consists of two exposures ($-45°$ and $+45°$ angles) of 5-min exposure time each. The sign of V/I is positive for all four data points (the sign distinguishes clockwise and anticlockwise circular polarization direction), and the circular polarization P_{cir} in per cent is therefore equal to the values in the third column. Uncertainties are 1σ.

Extended Data Table 3 | GROND optical and near-infrared photometry of the afterglow

Time since t_0 (mid; s)	g'	r'	i'	z'
11085.19	20.73 ± 0.08	19.80 ± 0.07	19.51 ± 0.07	19.25 ± 0.07
15496.95	21.09 ± 0.05	20.21 ± 0.07	19.84 ± 0.06	19.63 ± 0.07
17006.44	21.22 ± 0.05	20.31 ± 0.07	19.94 ± 0.06	19.68 ± 0.07
21430.12	21.45 ± 0.27	20.54 ± 0.07	20.20 ± 0.07	19.93 ± 0.09
106998.09	22.79 ± 0.24	21.99 ± 0.10	21.70 ± 0.12	21.48 ± 0.14
191934.13	23.31 ± 0.11	22.50 ± 0.09	22.13 ± 0.10	21.86 ± 0.13
2432398.02	24.24 ± 0.08	24.20 ± 0.09	23.80 ± 0.14	24.16 ± 0.15
Time since t_0 (mid; s)	J	H	Ks	
11085.19	18.67 ± 0.08	18.33 ± 0.09	17.96 ± 0.11	
15496.95	19.03 ± 0.07	18.70 ± 0.08	18.33 ± 0.10	
17006.44	19.07 ± 0.07	18.69 ± 0.08	18.56 ± 0.10	
21430.12	19.42 ± 0.08	18.90 ± 0.10	18.86 ± 0.13	
106998.09	20.99 ± 0.25	20.68 ± 0.30	20.29 ± 0.3	
191934.13	> 22.03	> 21.35	> 20.53	
2432398.02	> 22.50	> 21.92	> 21.02	

Magnitudes are as observed; uncertainties are 1σ; upper limits are 3σ.